Broatch, A.; Novella Rosa, R.; Gómez-Soriano, J.; Pinaki, P.; Som, S. (2018). Numerical Methodology for Optimization of Compression-Ignited Engines Considering Combustion Noise Control. SAE International Journal of Engines. 11(6):625-642. https://doi.org/10.4271/2018-01-0193

Numerical Methodology for Optimization of Compression-Ignited Engines Considering Combustion Noise Control

Author, co-author (Do NOT enter this information. It will be pulled from participant tab in MyTechZone)

Affiliation (Do NOT enter this information. It will be pulled from participant tab in MyTechZone)

Abstract

It is challenging to develop highly efficient and extremely clean engines, while meeting user expectations in terms of performance, comfort and driveability. One of the critical aspects in this regard is combustion noise control. Combustion noise represents about 40 percent of the overall engine noise in typical turbocharged diesel engines. The understanding of noise generation is intricate due to its inherent complexity and measurement limitations. Therefore, current efforts are focused on developing efficient strategies to understand the combustion noise mechanisms in order to reduce engine noise while maintaining high efficiency and low pollutant emissions. In the present work, a methodology was developed which combined computational fluid dynamics (CFD) modeling and genetic algorithm (GA) technique to optimize the combustion system hardware design of a high-speed direct injection (HSDI) diesel engine, with respect to various emissions and performance targets including combustion noise. The CFD model was specifically set up for reproducing the unsteady pressure field inside the combustion chamber, thereby allowing an accurate prediction of the acoustic response of the combustion phenomena. The model was validated by simulating several steady operation conditions and comparing the results against experimental data, in both temporal and frequency domains. The optimization goal was to minimize indicated specific fuel consumption (ISFC) and combustion noise, while restricting pollutant (soot and NO_x) emissions to the baseline values. An objective merit function was constructed to quantify the strength of the designs. Eight design variables were selected including piston bowl geometry, spray inclusion angle, number of injector nozzle holes and in-cylinder swirl. The in-cylinder noise level was characterized by the total resonance energy of local pressure fluctuations. The optimum engine configuration thus obtained, showed a significant improvement in terms of efficiency and combustion noise compared to the baseline combustion system, and limiting emissions within their respective constraints. This optimum configuration included a deeper and tighter bowl geometry with higher swirl and greater number of nozzle holes. Subsequently, a sequential analysis was also performed to assess the influence of each design parameter on different targets. This study demonstrated an effective way of incorporating combustion noise into a numerical optimization strategy for engine design.

Introduction

The worsening of the air quality due to the exhaust emissions of transport vehicles has increased the concern about the pollutant emission sources during the last decades. While the number of respiratory diseases has significantly grown in urban environments [1], the weather has experienced noticeable changes due to the global warming [2]. This situation has forced engine manufacturers to face ever-increasing exhaust emissions regulations whereas the strict customer demands aggravate the complexity of this regard.

As a consequence of this struggle, a variety of new combustion modes [3,4] have been developed. Most of them operate in highly premixed conditions to avoid particulate matter (PM) precursors while the nitrous oxides (NO_x) generation is controlled with large amounts of exhaust gases recirculation (EGR). A considerable number of investigations [5,6] have confirmed the suitability of these combustion concepts to achieve really low emissions of both NO_x and soot particulates, while keeping or even improving the engine performance. However, high pressure rates linked to these particular modes of combustion intensify the NVH (Noise, Vibration and Harshness) and thus compromise the user's comfort and the quality of life in populated areas [7].

Combustion noise is the result of the combustion and turbulence interaction [8]. The contribution of both phenomena in the overall noise emission may be completely different depending on the application. For instance, in compression ignition (CI) engines operating with conventional Diesel combustion (CDC), the pressure instabilities generated during the premixed combustion dominate largely the acoustic source, leaving pressure oscillations induced by the turbulence-combustion interaction [9,10] in a secondary role. Therefore, the knowledge about noise fundamentals is essential to assess the connection among the combustion and its corresponding acoustics.

In addition to the pressure instability induced by the combustion itself, the generated pressure waves resonate inside the chamber [11], thereby interacting with the chamber walls and behaving as an extra acoustic source. This complex phenomenon, commonly known as combustion chamber resonance, has a significant impact on the radiated engine noise because the characteristic excitation frequency span is in the highly sensitive human perception range [12,13] and its effects become especially evident during low-medium load and transient operation conditions [14].

Once the acoustic excitation occur, acoustic perturbations are transferred through the engine block into the vehicle and the environment. NVH analysis evidenced the complexity of propagation patterns of the acoustic energy [15]. Moreover, it allowed to stablish

a relation between the acoustic response of the engine and the block design as well as the acoustic insulation [16].

Hence, two different strategies are traditionally used to reduce the noise emissions and modify the acoustic signature of the engine so as to improve the impact on the user. The first, known as passive solutions, is related to the modification of the acoustic response of the source by combining a proper engine block design and encapsulation. The second strategy, denoted active solutions, consists in optimizing the hardware design and the operation settings to act directly on the combustion noise source.

Passive solutions have been thoroughly explored since the early eighties due to the inherent simplicity of the concept. Since the basis of this strategy lies attenuating the frequency contents which have an undesired effect on NVH, the unsteady mature of the acoustic response and its high non-linear behaviour complicates the understanding of the radiation paths and the involved mechanisms. Nevertheless, research efforts leaded to assess the acoustic radiation through simple models, establishing a relation between the combustion noise source and the end user. Anderton [17] proposed a linear behaviour between the source and the observer for the engine block attenuation curve. Even though this simplification does not allow for an accurate prediction of the radiated noise level, it is useful to perform comparative analyses, and several combustion noise metrics are defined following this method. More recently, other authors [18] found cause-effect relations between typical combustion related parameters and free-field noise measurements, allowing to connect the noise source with both the objective and subjective effects of engine radiated noise [12,13].

In contrast to passive solutions, the major difficulties in the active strategies reside in the understanding of the complex phenomena involved in the noise generation and their direct effects on the in-cylinder pressure field. This field demands multiple measurement points across the combustion chamber [19] for its recreation and subsequent analysis. Thereby it requires complex and expensive engine modifications. For this reason most authors resorted to perform numerical simulations in order to assess the noise source [20] instead. In particular, the use of computational fluid dynamics (CFD) is nowadays widely established in the automotive industry. Moreover, recent publications demonstrated that CFD is a useful tool to recreate, visualize and study the combustion noise source [21,22].

Despite the attractive benefits of this method, the simulation of an internal combustion engine is still nowadays one of the most challenging fields due to its complex geometry, spatially and temporally varying conditions and complicated combustion chemistry. Therefore, additional efforts must be focused on not only developing more robust codes, but also on the validation procedure to ensure a correct estimation of the involved physical phenomena [23].

Once the simulations have been validated, any number of parameters can be modified and quickly tested without high costs. This encouraged to explore additional techniques for the identification of the optimizing paths in the configuration chamber design [24] or in the operation settings [25,26]. The interest on optimisation methods based on Genetic Algorithms (GA) have increased in the automotive industry during the last years due to the wide range of solutions which may offer in a combination with CFD. Several authors [27,28] have applied this kind of techniques to diverse engine applications in which the number of optimizing parameters is relatively high. For instance, de Risi and Donateo [29] optimised the combustion chamber design of a CI Diesel engine with 6 design parameters considering emissions and performance. Sun and Wang [30] published a comparison between GA and artificial neural network for optimising the intake ports of a spark ignition (SI) engine with 4 parameters. In all these works, the computational cost appears as the main concern when applying this technique. Hence, the definition of a dynamic stop criterion for minimising the number of iterations is a key aspect to reduce the number of simulations and therefore the calculation time.

In this paper, a numerical methodology is implemented for optimising the combustion system in a high speed direct injection (HSDI) Diesel engine. Besides the performance and controlled emissions (NO_x and soot), engine noise is included as an objective parameter. In this way, special care is taken regarding CFD model features that can affect to the precise estimation of the in-cylinder pressure field, and subsequently, the noise emissions. Since one of the objectives of this paper is to contribute to the understanding of the relation between noise emissions and the chamber geometry in CDC, the final goal is to develop a reliable method suitable to be applied in new combustion modes such as Homogenous Charge Compression Ignition (HCCI) or Gasoline Compression Ignition (GCI) in different engine concepts and configurations.

The paper is organized as follows: first, the engine specifications characteristics are briefly described. Then, the numerical methodology is detailed, along with the validation of the CFD model. Subsequently, results were presented and discussed. Finally, conclusions about the methodology and its results are summarized, and further steps in the investigation are suggested for expanding its applicability.

Engine specifications and experimental facility

The configuration of the experimental facility is the same as that used in previous investigations [12,13]. The tests were carried out in a light-duty HSDI Diesel engine for automotive applications directly coupled to an asynchronous dynamometer. This is a 1.6 l, four-cylinder, turbocharged engine equipped with a common rail injection system. The main specifications of the engine and the injector are summarized in Table 1.

Table 1. Specifications of the real engine being modeled and injector system features.

Engine type	DI Diesel engine
Number of cylinders [-]	4 in line
Displacement [cm^3]	1600
Bore – Stroke [mm]	75.0 - 88.3
Connecting rod [mm]	13.7
Compression ratio [-]	18:1
Injector nozzles [-]	6
Nozzles diameter [μm]	124
Included spray angle [deg]	150

Test bench was installed inside an anechoic chamber which guarantees free-field conditions for frequencies above 100 Hz. In addition, the dynamometer was physically and acoustically isolated with sound damping panels to prevent possible disturbances in the noise measurements.

Additionally, the rate of heat release and other relevant combustion parameters were estimated by applying some simplifications to the energy equation [31].

Numerical methodology

In this section, the numerical methodology and the mathematical approaches outlined in the introduction are described in detail.

Numerical model setup

A virtual model of the engine was implemented in the commercial CFD code CONVERGE [32] for reproducing thermo-dynamic properties of the in-cylinder flow. The simulations were performed between two consecutive exhaust valve openings (EVO), encompassing a complete engine cycle. The numerical solution of the 3D domain was obtained by using the finite volume method and a second-order accurate spatial scheme.

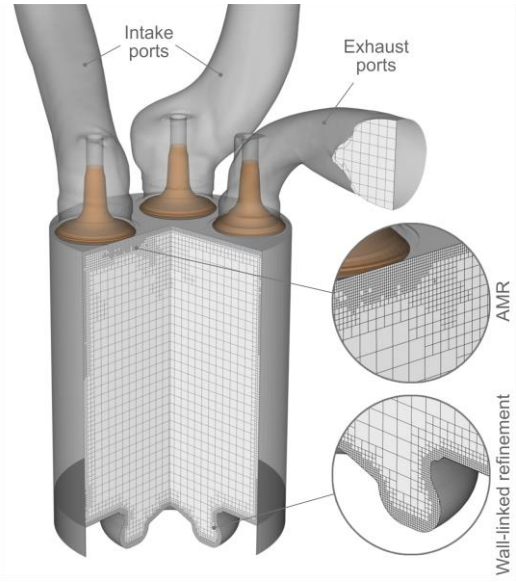

Figure 1. Computational domain at intake valve closing, including the intake and exhaust pipes and valves, cylinder walls and the combustion chamber on top of the piston. Details of the mesh sizing and its refinements at different zones are also provided.

The numerical domain, displayed in Fig. 1, included the complete single cylinder geometry and the intake-exhaust ports for performing complete cycle simulations. The mesh discretization was done by following the cut-cell Cartesian method available in the code. The base cell size was fixed as 3 mm in the whole domain. In addition, the original grid size was reduced in regions where the sub-grid field demands a higher resolution. Three levels of fixed grid refinement (0.375 mm of cell size) were therefore added to the walls of the combustion chamber, ports and in the spray regions in order to improve the boundary layer prediction and the precision in the modelling of chemical reactions and spray properties (atomization, break-up, coalescence, etc.). The base mesh size of the chamber is also reduced with two levels of grid refinement (0.5 mm of cell size) after the start of the combustion for an improved recreation of the interaction and reflection of the pressure waves. The code also uses an adaptive mesh refinement algorithm (AMR) to increase the spatial resolution (up to 0.378 mm of cell size) where both velocity and temperature gradients are sufficiently meaningful. Thereby, the total number of cells depended on the simulation timing and varied between $1.5 \cdot 10^6$ cells at Bottom Dead Center (BDC) and $0.5 \cdot 10^6$ at Top Dead Center (TDC). This mesh configuration was achieved after a grid independence study, offering a mesh-independent solution for the pertinent acoustic and combustion parameters.

The sonic Courant number, based on the speed of sound, were fixed to one during the combustion to capture local fluctuations of the in-cylinder pressure field. Several monitor points were distributed across the combustion chamber in order to analyze the location of the standing waves. Moreover, the computed pressure was recorded at a sampling frequency of 50 kHz so as to provide an aliasing-free bandwidth sufficient to cover the human hearing range [33].

The turbulent flow properties were approached by the renormalization (RNG) model [34] coupled with a heat transfer approach [35]. This approach has been successfully used in many numerical simulations of compression-ignited combustion presented in the literature, [36,37]. Coupled with appropriate combustion models, Wright et al. [38] demonstrated that this turbulence model allows accurate reproduction of autoignition, while Han and Reitz [39] established that realistic rates of heat release can be achieved. The Redlich-Kwong equation [40] was selected as the equation of state required for calculating the compressible flow properties and the pressure-velocity coupling was achieved by using a modified Pressure Implicit with Splitting of Operators (PISO) method [41].

Regarding the combustion, it is approached through a direct integration of the surrogate fuel chemical mechanism [42]. The chemical mechanism was based on a Primary Reference Fuel (PRF) blend of n-heptane and iso-octane, deactivating the iso-octane reactions so as to predict the diesel ignition features. The reaction mechanism was derived from the ECR-Multichem mechanism [43] and it was formed by 42 species and 168 reactions. The fuel injection was approached by the standard Discrete Droplet Model (DDM) [44] and the spray properties were simulated by the Kelvin-Helmholtz Rayleigh-Taylor (KHRT) model [45].

Wall temperatures were assumed isothermal and estimated by using a lumped heat transfer model [46]. The inflow/outflow boundaries placed at the end of the intake and exhaust ports were established from the average value of instantaneous pressure and temperature measurements.

Finally, the return time for a full-single cycle simulation, 720 crank angle degrees (cad), was about 130 hours when the calculation was distributed on 32 cores.

Validation

Four different steady operation conditions, summarized in Table 2, were selected to validate the numerical model. In order to ensure that this sample is enough representative of all noise issues present in the whole operation range, the contribution of each frequency band (low, medium and high frequency) to the overall engine noise was completely different in each operation point.

Traditional in-cylinder pressure measurements through a single transducer do not provide enough information for evaluating the effects of the resonance due to the local fluctuations of the pressure field. Broatch et al. [21] proposed a methodology based on CFD simulations to overcome this limitation without complex and expensive engine modifications. They compared the simulated and

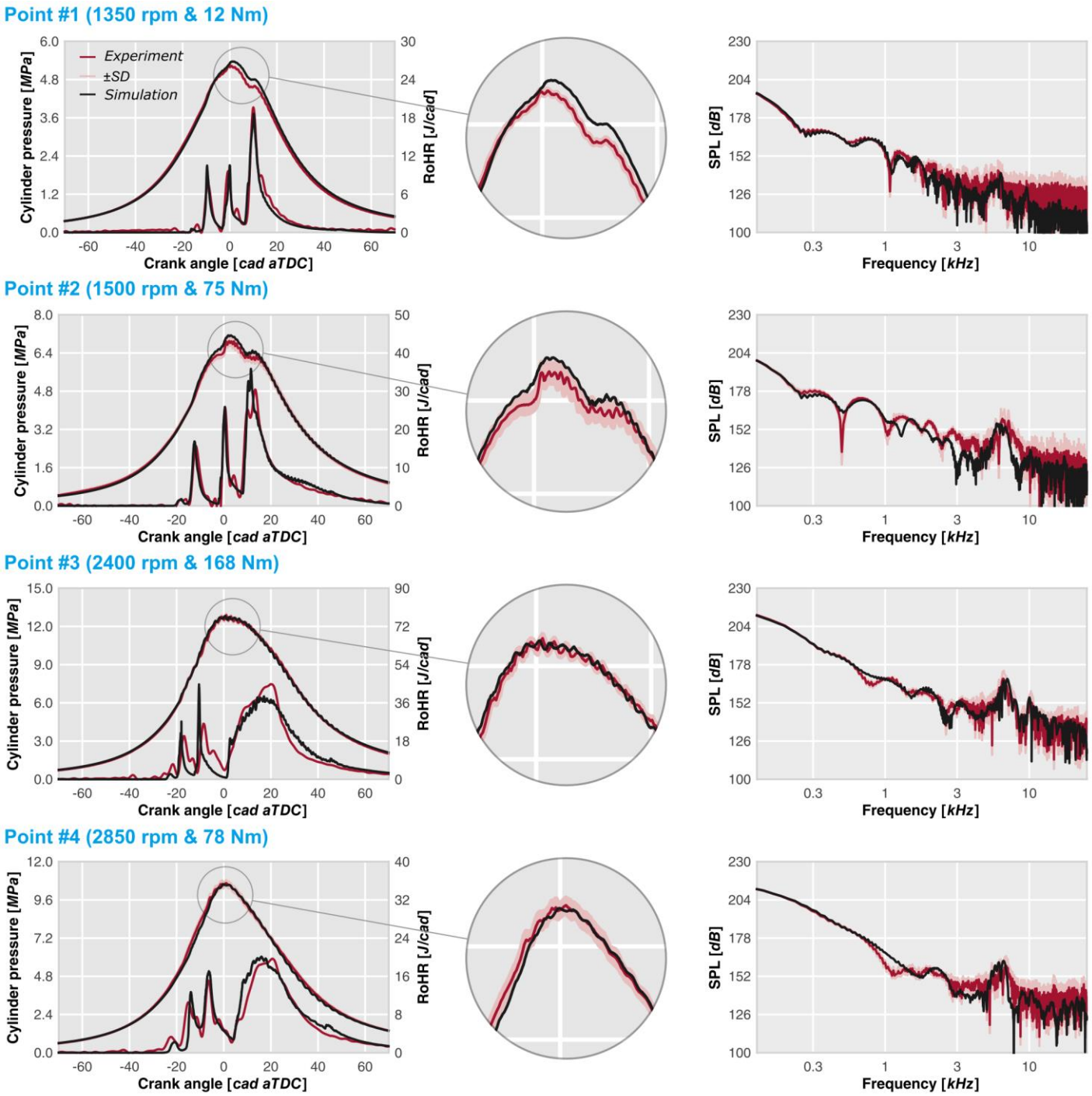

Figure 2. Results of the qualitative validation analysis. The pressure signals registered at the transducer location are shown together with the estimated RoHR (left side) and the pressure spectrum (right side). The standard deviation (SD) of the measured cycles is included in order to compare the numerical solution with the measurement dispersion due to cycle-to-cycle variations.

measured pressure profiles at the same location of the pressure transducer and checked the consistency between numerical results and measurements in both the time and frequency domains. Then, the solution can be considered suitable for extrapolation to the entire domain. They also defined an elaborate procedure for choosing a representative cycle of a specific operation point. This method was specifically developed for preserving the high frequency content of the pressure signal after the cycle averaging. The resulting cycle is therefore the most representative of the noise generated during a specific engine test.

Figure 2 shows the results obtained after the end of simulations for comparison against experiments. On the left side, pressure traces registered at the transducer location in experiments and simulations are plotted. In general, a good match among both pressure traces is achieved in all cases. Zoomed views also show how the resonant

oscillation process is consistently reproduced. On the other hand, the pressure spectral density or sound pressure level (SPL) of all operation points is displayed on the right side. Estimations coincide with the measurements in almost the whole frequency range and operating conditions, with only a slight disagreement being observed for the medium frequencies in points #2 and #4.

Table 2. Output parameters and main engine settings of the modeled operation points for the model validation.

Test ID	**Point #1**	**Point #2**	**Point #3**	**Point #4**
Engine speed [rpm]	1350	1500	2400	2850
Torque [Nm]	12.3	75.2	168.3	87.0
Num. injections [-]	3 (2 pilots + main)			
Inj. pressure [MPa]	40	87	80	92
Intake pressure [MPa]	0.104	0.118	0.206	0.181

Besides to the in-cylinder pressure comparison, the rate of heat release (RoHR) is also included in Fig. 2 (left side) for deeper validation of the combustion process. The experimental RoHR is obtained by solving the energy equation by direct measurements and assuming several simplifications [31]. Again, the simulated data reasonably agrees with the experiments.

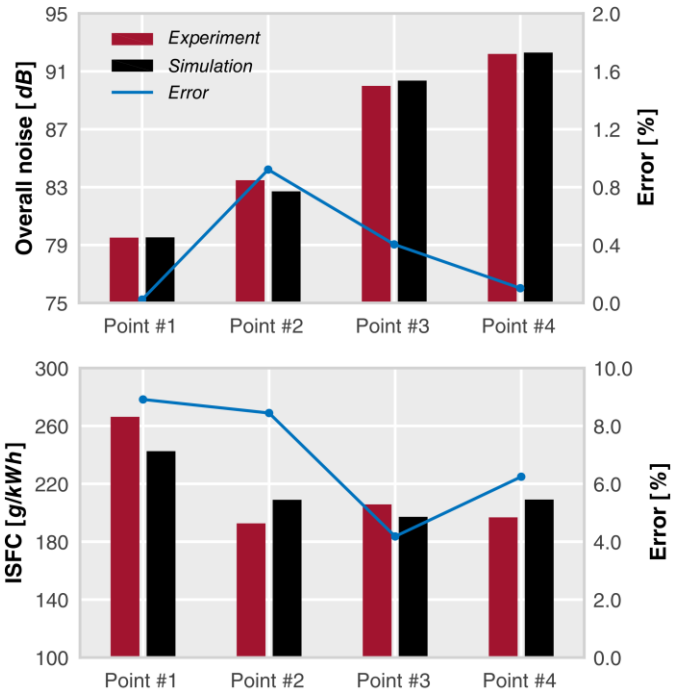

Figure 3. Results of the quantitative validation analysis. The numerically estimated values of the overall noise (top) and ISFC (bottom) are compared against those obtained by the measurements.

The suitability of the model for predicting noise emissions and performance levels adequately was also checked. The Overall Noise (ON), further explained at Appendix, and the ISFC metrics were selected for this aim. Fig. 3 shows that both ON and ISFC predictions are good, since errors between the simulations and experiments are below 1% and 10%, respectively. Thus, although the slight disagreement in the medium frequency range of the spectrum of some operation points, the model ensures an accurate prediction of the external engine acoustic field in all considered conditions. In the same way, the estimations of the ISFC may be regarded as good.

Simplified approach

Despite the coherence between simulations and experiments observed above, the CFD model is highly time consuming. This makes the model a reliable tool for analyzing the relation among the combustion and its correspondent acoustic effects but also compromises its applicability to mathematical techniques, such as genetic algorithms, that autonomously refine a solution until an optimum is found through massive calculations.

Several modifications to the original model setup were consequently done for minimizing the calculation time while the accuracy is maintained as high as possible.

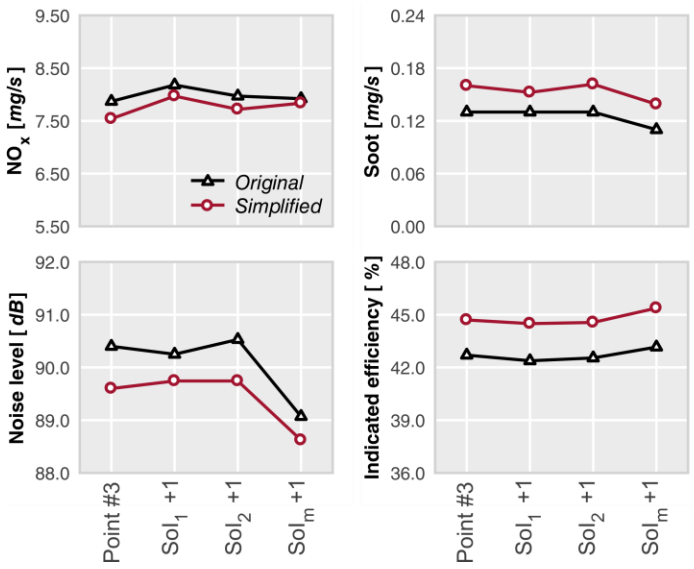

Figure 4. Coherence analysis of the simplified model. The solutions (emissions and ISFC) of the simplified model are compared against the original model setup. The injection settings of point #3 were modified by increasing the start of each injection (SoI): first pilot (1), second pilot (2) and main (m) injections.

First, the base cell size were enlarged up to 5 mm. All fixed embedding regions were maintained with the same levels of grid refinement. That means that walls, spray and AMR regions have a minimum cell size of 0.625 mm whereas the resolution of the mesh in the chamber is reduced to 1.25 mm during the combustion event.

Second, the sonic Courant number were fixed to 2 during the combustion instead to enlarge the time step.

Finally, the simulation time was limited to the close cycle, encompassing only the time between the intake valves closing (IVC) and EVO. Furthermore, the calculations were initialized by a non-uniform spatial distribution of thermodynamic conditions and species concentration. These were obtained by a previous simulation of the gas exchange process (GEP) using the baseline engine configuration. Although the calculation time is considerately reduced with this measure, the conditions at IVC may notably change when the combustion chamber is modified. In view of this, a preliminary analysis was carried out to check the accuracy of the simplified

model. In this case, nominal injection specifications at point #3 were varied to reach significant changes in emissions and ISFC levels. Fig. 4 presents the results of this study. It is clearly observable how the simplified model does not predict the exact value of all considered parameters. However, trends are properly reproduced, showing a high level of coherence with the original model solution.

These modifications allow to reduce the calculation time in almost 80% while a correct reproduction of the observed trends in the most relevant parameters are guaranteed. Nevertheless, any solution obtained by this simplified approach must be verified by the original model simulation.

Optimization method

The combustion system optimization were performed using a genetic algorithm approach, framed whiting the evolutionary methods group. These methods have been demonstrated a great suitability for finding the optimum solution of complex multivariable problems related to engine optimization, such as combustion chamber [47] or intake ports design [29].

Since there are many different styles of GA, the main basis is common to all of them. The mathematical algorithm attempt to imitate the natural evolution by generating a population of candidates, or generation of citizens, which are subjected to a quality test. The best candidates are then selected to produce a new generation of citizens with the optimal traits of them. In addition, it incorporates random variations of the best traits in order to mimic aleatory genetic mutations viewed in nature. Differences reside in which mathematical approaches are used to mimic these regards. In the GA used in this work, each generation is built by using the Punnett diagram [48] where the best five citizens of previous generations become the parents of the new generation. Consequently, the size of the population depends on the number of parents and is equal 25 citizens.

Once the generation is created, each chromosome (optimizing parameter) of every citizen is then mutated. The original value of the chromosome was adjusted by a normally distributed random number. The standard deviation of this random distribution is exponentially reduced as the genetic algorithm progresses, thereby causing that the mutation rate decays. This approach allows to explore the whole design space in the early steps of the GA, whereas in the final generations the solution is forced to converge.

As commented before, the main target of this optimization procedure is to reduce the combustion noise without penalties in the efficiency. Recent studies [49] have shown two different paths to deal with the combustion noise issue by using active solutions. The first strategy consists on decreasing the maximum rate of pressure change by promoting smooth premixed combustions. As a counterpart, the inherent relation between the rate of pressure change and the cycle efficiency could compromise the performance. The other strategy is based on controlling noise by reducing the contribution of resonance phenomena. This shows an attractive advantage when it is compared with the previous one: the independence from cycle efficiency. The optimization was therefore approached by following the latter point of view in which noise emissions are reduced by the effect of the resonance lowering. Hence, the operating point #3, used in the validation section, was selected as baseline for optimization, since this point exhibit the highest value of the resonance energy.

In order to be consistent with the second strategy, the energy of resonance (E_{res}), documented in the Appendix, and ISFC were fixed as the two main parameters to minimize by the GA. In addition, NO_x and soot emissions were considered constraints. Thus, citizens whose surpass the constrained levels are accordingly penalized. All these premises were mathematically expressed in form of a merit function (MF) as

$$MF = \frac{0.3481 \cdot \sum_{n=1}^{2} \alpha_n}{\sum_{n=1}^{2} \left(\alpha_n \cdot e^{\beta_n \cdot \frac{x_n - x_n^{target}}{x_n^{target}}} \right)} - \sum_{n=3}^{2} \left(\max\left(1, \frac{x_n - x_n^{limit}}{x_n^{limit}}\right)^{\gamma_n} - 1 \right)$$

$$x_1 \longrightarrow E_{res} \qquad x_2 \longrightarrow ISFC \qquad x_3 \longrightarrow NO_x \qquad x_4 \longrightarrow soot \tag{1}$$

where x_n is the value of each parameter at a given configuration, x^{target} is an optimistic estimation value of both objective parameters while x^{limit} stands for the emission levels achieved by the baseline specifications, finally, α_i, β_i and γ_i are weighted constants for specifying the influence of each parameter in the merit function. Table 3 displays the constants and reference values considered in this study.

Table 3. Summary of the constants and reference values of the merit function. All these parameters were obtained by taking into account a previous sensitivity analysis and several simulations with baseline specifications.

Parameter	**E_{res}**	**ISFC**	**NO_x**	**Soot**
α_i	3.0	2.0	-	-
β_i	2.0	2.0	-	-
γ_i	-	-	15	0.5
x^{target}	0.1 kPa^2s	150 g/kWh	-	-
x^{limit}	-	-	7.54 mg/s	0.16 mg/s

Eight parameters related to the combustion system design were chosen as inputs for the GA. Five of them were referred to the combustion chamber geometry, two were related to the injector configuration and the last one alluded to the intake ports design.

The generation of realistic and coherent combustion chamber designs was one of the most complex steps in this procedure. Chamber geometries may be so different and intricate that complicate its recreation with only a few parameters. Here, a bowl profile generator were implemented using Bezier polynomial curves and five optimizing parameters [24]. As can be seen in Fig. 5, this method offers a wide range of possible chamber designs, from large-open bowls to thigh and highly reentrant ones. The only restriction assumed for the chamber generation was the compression ratio, which was set to be the same as in the baseline specifications. The compression ratio was therefore kept by adjusting the free squish height. However, in some cases the proposed geometry can't match with the specified compression ratio, then the geometry was discarded and a distinct set of random mutations were applied to these particular geometric parameters.

The two aspects to optimize in the injector configuration were: the included spray angle to guide the fuel within the bowl, and the number of injector nozzles. In all cases the injection rate remained

fixed while the total injection area was kept constant. This means that nozzle diameters of the injector holes were adapted to maintain the overall injection area, assuming that the discharge coefficient remains constant for every hole. Therefore, the nozzle diameter was decreased as the number of nozzles were increased.

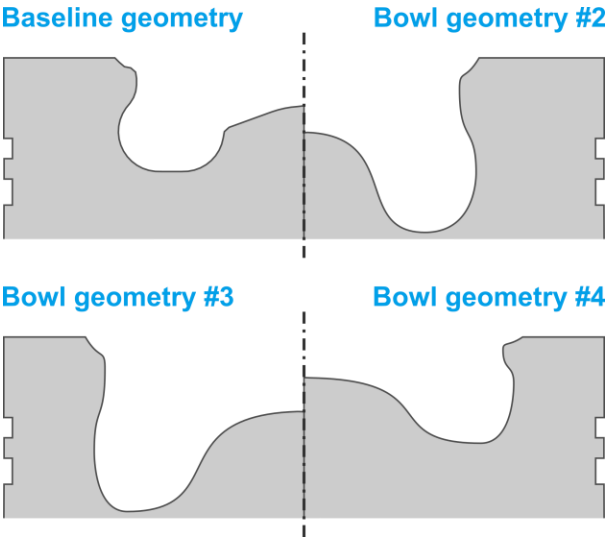

Figure 5. Example of different bowl profiles obtained by the Bezier polynomial method [22].

The design of intake ports were indirectly optimized by considering the swirl number at IVC as an optimizing parameter in the GA loop. The non-uniform conditions of velocity used for the calculation initialization were accordingly adjusted for reach a given value of swirl number.

Results and discussion

In this section, data resulting from the optimization procedure are presented and discussed. First, the convergence of the GA is verified and trends of the output parameters are analyzed. Then, the coherence of the results between the simplified and original model setups is inspected. Finally, the outputs of the optimized configuration are compared against the baseline and in-cylinder acoustic effects are analyzed in detail for contributing to the comprehension of noise generation mechanisms.

Optimization results

Before starting with the analysis of GA results, verification of the algorithm convergence is the first required step to ensure that the solution meets a unique solution.

Although the algorithm convergence is mathematically determined, since the mutations variability is reduced as the GA progresses, the attainment of the best solution after a given number of generations defined a priori is not guaranteed. For this reason, the progression of the merit function as the GA progresses is included in Fig. 6. Besides to MF values of every simulation, the generation averaged value and the generation dispersion (±SD) are also included in the graph. It can be seen that the average and dispersion are significantly reduced after the 12th generation. Nevertheless, the solution continues to improve even after the 20th generation. At this point, the average remains practically constant until the final generation. The dispersion however keeps oscillating till the 27th generation, where it remains reasonably constant up to the final generation. Observing this progress, the optimization was stopped at 29th generation after three iterations without remarkable changes in both parameters and the solution was considered converged.

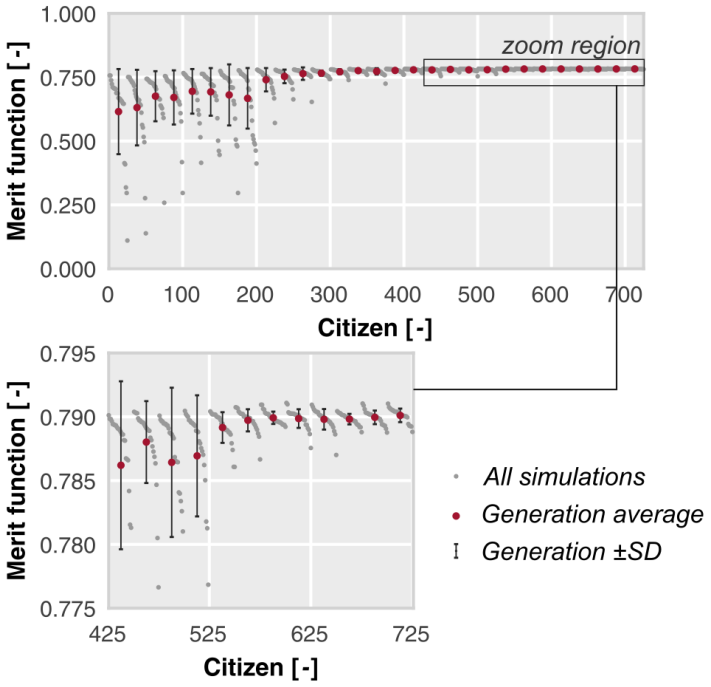

Figure 6. Evolution of the merit function value as the genetic algorithm progresses. An acceptable convergence is achieved after 29 generations.

Subsequently, the inspection of the target and constraint parameters is the following natural step in order to check the solution success and constraints compliance. Fig. 7 show the progress of these parameters along the optimization procedure. The top graphs show how both constraints tend to the restricted values, reaching a final solution which practically coincides with these values. The middle graphs show notable improvements in both objectives: while the energy of resonance is reduced in almost 70%, the ISFC exhibit an improvement of 2%. The bottom plots are included to illustrate how these enhancements affect to the overall noise and indicated efficiency. It is observed how noise emissions are reduced by acting directly to the resonance phenomena whereas the efficiency is even increased. This fact confirmed the suitability of the strategy described in the previous section for decreasing noise emissions [49].

Table 5. Comparison between the baseline and optimized specifications. All relevant parameters are included to observe the main changes in the engine outputs.

Configuration	**Baseline**	**Optimized**
E_{res} [kPa^{2}s]	5.95	1.53
ISFC [g/kWh]	188.3	184.9
NO_x [mg/s]	7.54	7.48
Soot [mg/s]	0.16	0.12
Overall noise [dB]	89.6	88.2
Indicated eff. [%]	44.7	45.5

In addition to the general trends observed in these parameters, in Table 5 it is included a comparison among the baseline and optimized specifications so as to quantify the maximum improvement of all relevant output parameters. As observed in the previous trends, the energy of resonance show the maximum lowering, so the overall noise is reduced by more than 1dB. Moreover, efficiency levels increase 0.8 points whereas both pollutant emissions are maintained below the baseline levels.

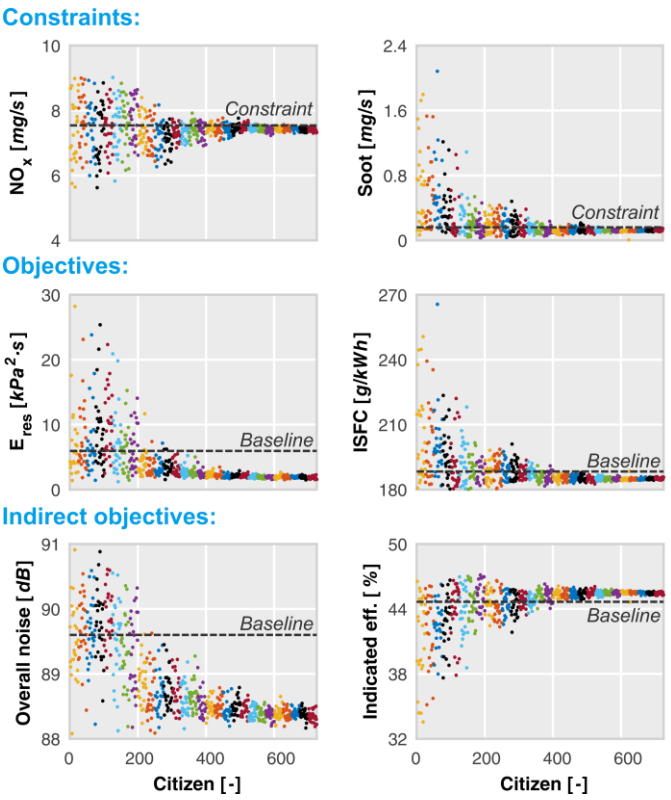

Figure 7. Progress of objectives and constraints towards the optimum solution. The final targets (indirect objectives) of the optimization are also included.

Another interesting point is to examine the optimized configuration for determining which design parameters have changed to a greater extent. Hence, all contemplated parameters of both specifications are included in Fig. 8 for comparison. The optimized geometry exhibit a deeper and tighter bowl profile with a less reentrant shape. Furthermore, changes in the injector configuration and intake ports design are directed to enhance the mixing rate and to minimize the spray penetration, avoiding thus an excessive wall fuel impingement during the injection event. The number of injector nozzles increases up to 12, as a result the diameter of nozzles is also reduced. Finally, the included spray angle is expanded 13.4 degrees while the swirl number slightly grows.

Coherence of the results

In the previous section, a certain number of modifications have been applied to the original model setup in order to reduce the calculation time for the optimization. Although results of this modified model were considered sufficiently accurate, since it captures the main trends of the original solution, the coherence of this solution must be verified by simulating the optimized system in the original model setup.

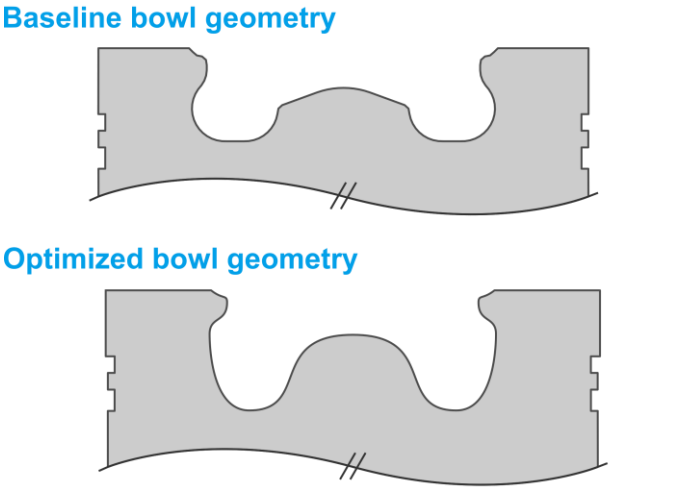

Configuration	**Baseline**	**Optimized**
Included spray angle [deg]	75.0	83.4
Number of nozzles [-]	6	12
Swirl number [-]	1.26	1.69

Figure 8. Comparison of the baseline and optimized configurations. Baseline bowl profile is plotted together with the optimized bowl geometry (top) whereas the injector and flow motion parameters are showed in the table (bottom).

Therefore, a series of consecutive engine cycles using the optimized configuration were calculated with the original mesh size (3 mm) and fixing the sonic Courant number to 1. As the intake ports design was indirectly optimized by the swirl number achieved after the GEP, the velocity field was adjusted every IVC to achieve the swirl number demanded by the optimized design. Following this approach, it is possible to modify the swirl motion during the combustion without intake pressure changes, thereby allowing a fair comparison among both combustion systems. It is thus assumed that the new intake ports design reach a high swirl motion with the same intake pressure.

After the third cycle the solution was considered converged, since the pressure trace and spectrum registered at the transducer location did not show any relevant dispersion.

Table 6 summarizes the obtained results for both model setups with both combustion system designs. It is appreciated how the simplified model causes the same effects on the solution in both designs. Every parameter which is overestimated in the baseline design (soot and indicated efficiency levels), it is also overestimated in the optimized one. In the same way, this behavior is also replicated in every underestimated parameter (NO_x and overall noise levels). This fact evinces the consistency among both numerical models, since they reproduce the trends even when the system configuration is completely modified.

Apart from this, the change of NO_x, soot and efficiency levels shows a great similarity. For instance, NO_x emissions vary 0.33 mg/s in the baseline specification whereas the change in the optimized one is 0.37 mg/s.

However, this difference is noticeably higher in noise levels. While it is around 0.8 dB in the baseline, the optimized configuration shows a

1.6 dB of change. As Broatch et al. and Torregrosa et al. emphasize in several publications [21,22,49], local thermodynamic conditions before the ignition are determinant in the combustion and its subsequent in-cylinder pressure field effects. Therefore, limiting the simulations to the close cycle and initializing the calculation with the results of the previous GEP using the baseline configuration, could affect to the prediction of noise levels when the geometry is highly modified, since local thermodynamic conditions may notably change.

Despite this slight weakness, the simplified solution offers a good prediction of main parameters and it allows to reach the optimization objective: it gives a combustion system configuration which reduces noise emissions while pollutant emissions and efficiency levels are maintained. Thus, even not being perfect in terms of prediction, the proposed approach is a reliable tool for accounting the combustion noise of CDC in optimization methods.

Table 6. Coherence of the results obtained by the simplified and original model setups.

Setup	**Simplified model**		**Original model**	
Configuration	**Baseline**	**Optim.**	**Baseline**	**Optim.**
NO_x [mg/s]	7.54	7.48	7.87	7.85
Soot [mg/s]	0.16	0.12	0.13	0.10
Overall noise [dB]	89.6	88.2	90.4	89.8
Indicated eff. [%]	44.7	45.5	42.7	43.6

Emissions analysis

In this section, an analysis of pollutant emissions (NO_x and soot) is performed with the intention to understand their behavior in face of the new combustion system. This study uses the solutions of the original model setup to increase the integrity of the results and therefore the soundness of the conclusions.

Although emissions levels are practically the same in both specifications, not necessarily implies that they evolve in the same way during the cycle. Consequently, the production and later oxidation of these pollutants may change. For instance, examination of Fig. 9 show how soot mass follows different paths as the combustion progresses. The maximum amount of soot is clearly inferior in the optimized configuration. It seems that this design enhances the mixing rate, reducing the soot production.

In Fig. 9 (bottom) it is also included the equivalence ratio distribution as a function of fuel mass evaluated at 24 cad aTDC, just where both traces start to differ. This graph show that the fuel mass within the soot production region ($\phi > 2$) is substantially decreased compared to the baseline, thereby explaining the lower production of soot in the optimized configuration. Nonetheless, the optimized design is not able to oxidize the same amount of soot than the baseline, matching the same levels of soot at the end of the close cycle. This particular behavior is probably caused by the shortage of oxygen within the bowl due to its extremely deep design.

Otherwise, as can be seen in Fig. 10, NO_x mass barely exhibits differences between both configurations and only slight differences can be observable during the combustion of the pilot injections.

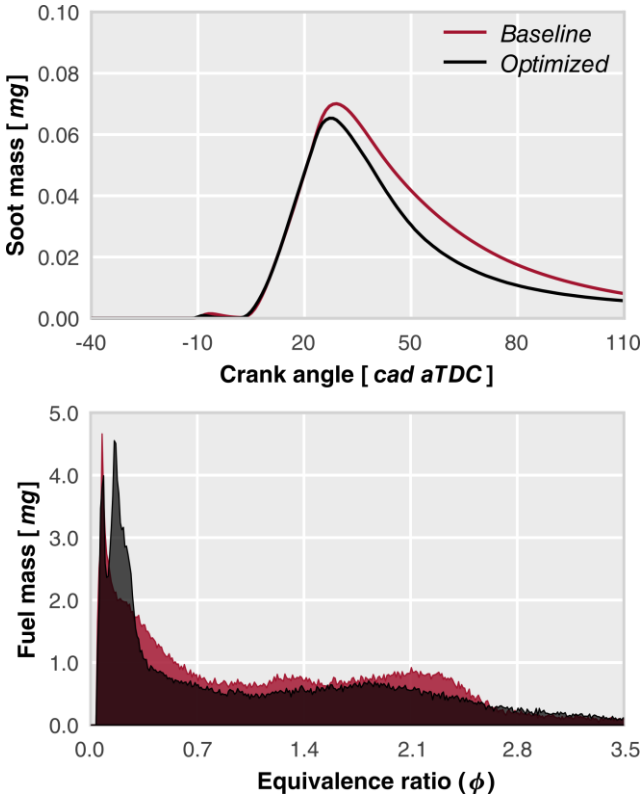

Figure 9. Soot mass as a function of the crank angle for both combustion system specifications: baseline and optimized (top). Analysis of local conditions evaluated at 24 cad aTDC. The equivalence ratio distribution as a function of fuel mass is included again for both configurations (bottom).

Acoustics analysis

In addition to consider combustion noise control in optimization strategies, the other interesting aspect of this investigation resides on reproducing the pressure oscillations that are present in a real engine and are responsible for resonant combustion noise. The comprehension of such complex issue could suppose an important step in the combustion noise control.

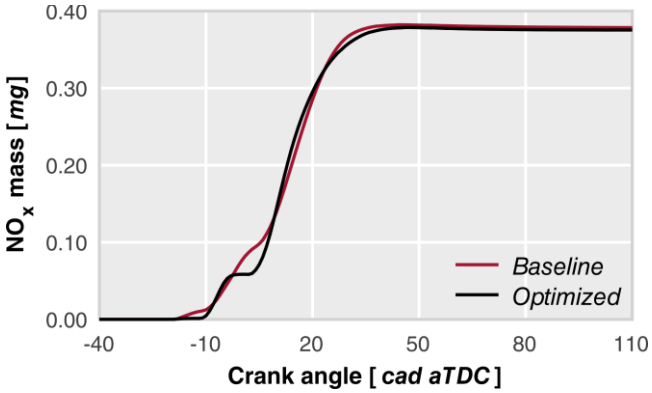

Figure 10. NO_x mass as a function of the crank angle for both combustion system configurations: baseline and optimized.

The numerical pressure data available after the simulations, once validated, can then be analyzed through different techniques to reveal the real behavior of the in-cylinder pressure field, thus providing

valuable information about pressure oscillation modes, their characteristic frequency and their temporary evolution. However, the complexity of resonant acoustic field complicates even a simple recreation for visualization purposes and it thus hinders a correct interpretation of involved phenomena.

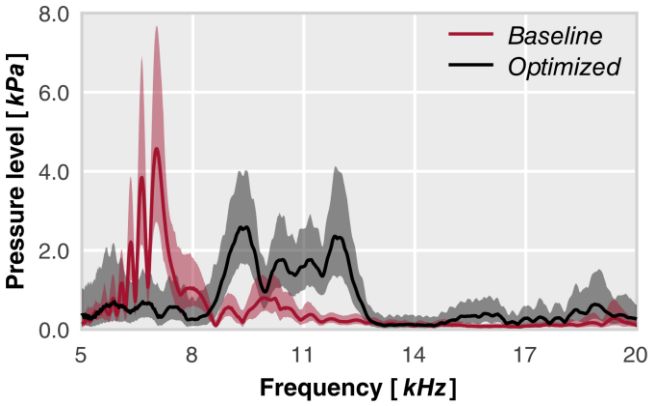

Figure 11. Comparison of the in-cylinder pressure spectra trends. The pressure spectrum averaged over all cell in the domain is plotted with its standard deviation (±SD) for both configurations (baseline and optimized).

For this reason, most of acoustic related publications focus on performing basic and straightforward studies which are based on qualitative comparisons of the acoustic field [50] or traditional acoustic metrics [51]. Only a few of them try to link the frequency content with the spatial energy distribution [22] or the time evolution [52] in an effort to understand propagation and dissipation patterns.

A way to explore the spatial distribution of the acoustic pressure field for different frequency phenomena of interest is to perform the Fourier transform (FFT) at each cell record in the considered domain. Then, the dispersion of high frequency spectra gives an idea, at least in a qualitative way, about the variability of the pressure field along the combustion chamber. Fig. 11 exemplifies this procedure, the averaged pressure spectra are plotted together with the spatial variation, represented by the standard deviation (±SD), for both specifications considered so far. Interesting information can be obtained about the most excited modes though. It seems that the acoustic energy is shifted toward higher frequencies in the optimized configuration. Consequently, new resonant modes experience a notable amplitude lowering, causing the reduction of the overall resonant noise. Also, the spatial variability is reduced in those frequencies in which modes are attenuated (6-8.5 kHz) and, conversely, it is increased at the harmonics with higher level of excitation (8.5-13 kHz and 15-20 kHz).

Since this information sheds some light about the internal pressure field, it becomes impossible to imagine how this field is locally changing given the limitations of this method. Some authors have taken a step forward by combining FFT, band-pass filtering and multiple monitors allocated in the combustion chamber [21] in order to overcome these limits. However, they are still missing the temporary evolution of each acoustic mode. The use spectrograms can be useful in this affair but again the spatial distribution is vanished. Therefore, none of these methods has the capacity to connect three domains involved in the resonant noise regard (space, time and frequency), evincing the necessity of a more sophisticated technique for giving a global vision of this issue.

The number of publications related to the modal decomposition of the unsteady flow fields is increased significantly [53,54,55] during the last years. In particular, the Proper Orthogonal Decomposition (POD), also called Principal Component analysis (PCA) or Karhunen–Loève expansion [56], is one of the most used due to its suitability for identifying which spatial structures comprise the most energy of the flow field. This method decomposes the flow into both spatial and temporal orthogonal modes whereas frequency components of these modes can be obtained by FFT application. Thus, once the method is applied, a complete connection between spatial, temporal and frequency domains is achieved.

Although some authors have specifically addressed ICE combustion issues through POD, these studies have been focused on cycle-to-cycle variation analysis [57,58], spark ignition misfires [59] or the evolution of a particular species [60]. Only Torregrosa et al. [61] have applied this method to acoustic issues of combustion chambers.

Taking this work [61] as a reference, a POD analysis of the in-cylinder pressure field was carried out to address the limitations of previous methods commented above. Orthonormal POD modes (Ψ_i) and their corresponding energy of excitation (obtained from their principal values σ_i) were obtained, together with temporal evolution coefficients (a_i).

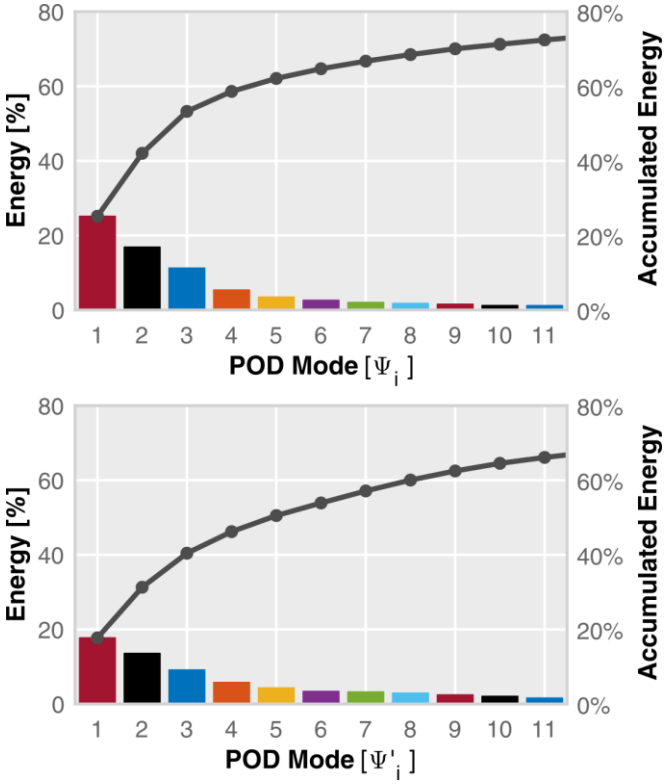

Figure 12. Pareto charts showing the energy contribution of POD modes $\Psi_{1\text{-}11}$ and the accumulated contribution to the resonance energy in each configuration: the baseline (left) and the optimized (right).

In order to characterize the relevance of each mode, their contribution to the total energy is analyzed. Then, the resonance energy of both designs is distributed as shown in the Pareto charts of Fig. 12. It can be seen in this figure that POD modes $\Psi_{1\text{-}11}$ gather approximately 70% of the resonant energy, with 50% being gathered just by modes $\Psi_{1\text{-}5}$. Although not shown in the graph, 80% of the remaining energy

is represented by modes $\Psi_{1\text{-}26}$ and finally modes $\Psi_{1\text{-}179}$ sum up to 99%. The rest of the modes represent just 1% of the remaining energy. Besides, the baseline shows that first three modes ($\Psi_{1\text{-}3}$) concentrates the major part of this energy while the distribution of the optimized configuration is more equitable.

The spatial distribution of the POD modes can be inspected, by plotting data available after the method application. The pressure amplitude associated with each set of coordinates is plotted in Fig. 13 using a set of isosurfaces. POD modes $\Psi_{1\text{-}5}$ were thus displayed by showing the upper and lower 10% tails (this is, the 10% and 90% percentiles) of the distribution of their amplitudes. In this figure, red and blue volumes thus indicate the distribution of the top 10% positive and negative amplitudes of the mode, so if the mode shape was animated by plotting the red and blue volumes would identify the regions oscillating with alternating higher amplitudes. In the same way, the nodal regions which amplitude remains mostly constant in time, correspond with the empty volume regions. The five most energetic modes were solely included in the analysis since they exhibit the most meaningful differences among both designs.

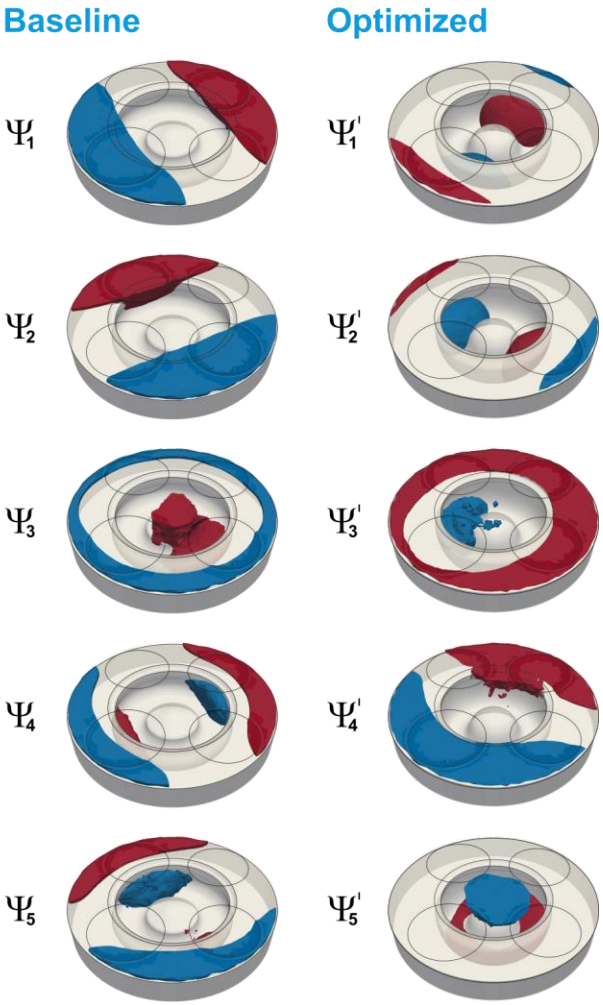

Figure 13. Spatial distribution of POD modes $\Psi_{1\text{-}5}$ across the simulated combustion chamber. Each mode is represented by colored isovolumes indicating the 10% (blue) and 90% (red) percentiles of the distribution of the real values of each individual mode.

Inspecting the shapes of modes Ψ_1 and Ψ_2 in Fig. 13 it is clearly seen how the higher amplitudes are oscillating on opposite sides of the squish zone, in two different orientations. Furthermore, it can be seen that these two modes are reminiscent of classical acoustic transversal modes in opened combustion chambers, specifically mode (m = 1, n = 0) in the notation of Hickling et al. [20], also called first asymmetric mode. In contrast to these, POD mode Ψ_3 features a completely circular distribution between the squish zone and the bowl, with an annular nodal region instead of a straight one like in the previous modes, being similar to Hickling's first radial mode (m = 0, n = 1).

There is another interesting aspect in Fig. 13 which can provide additional information about the resonant modes behavior. It can be seen how the spatial distribution of the most energetic modes are remarkably different in both engine configurations.

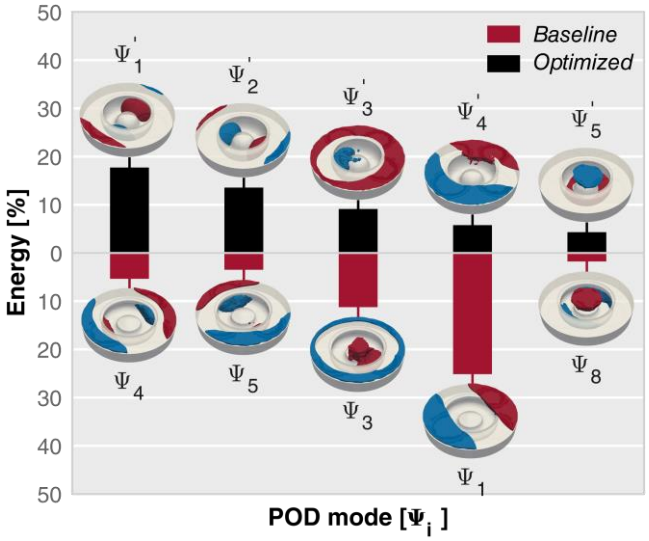

Figure 14. Energy share and spatial distribution of the five most relevant optimized design modes $\Psi'_{1\text{-}5}$ (top), together with their most closely resembling baseline counterparts (bottom).

Recalling the energy distribution of the modes plotted in Fig. 12, in Fig. 14, the energy share and spatial distribution POD modes $\Psi'_{1\text{-}5}$ are plotted, along with that of the most closely resembling mode of the baseline ($\Psi_{1,3,4,5,8}$). This figure shows how the modal energy has shifted from the original to the modified combustion, thus how the spatial distribution of the unsteady pressure fluctuations has been affected by the new design. It can be seen that $\Psi'_{1\text{-}2}$ modes which were previously ranked fourth and fifth with 5.36% and 3.48% of the energy, are now the most relevant with an energy share of 17.73% and 13.57%, respectively. Modified mode Ψ'_3 are shown to closely resemble the original Ψ_3 mode. Its energy content on the other hand have been slightly diminished. Finally, the original bowl-dominated mode Ψ_8 has been promoted to the fifth place with almost three times its previous energy. Therefore, it is possible to claim that the transfer of the resonant energy to higher frequencies, which was observed in Fig. 11, is also accompanied by a change in the spatial distribution of the pressure field.

The information contained within POD data also allows the analysis of the evolution of each mode in the time and frequency domains. In Fig. 15, the frequency content associated to $\Psi_{1,4,8}$ and $\Psi'_{4,1,5}$ modes is presented. It is evident that each POD mode is associated to a

specific frequency band. These modes were specifically selected to illustrate the effects described in Fig. 11. For instance, modes Ψ_1 and Ψ'_4 clearly mimic the reduction of the pressure spectra gathered between 5 and 8.5 kHz. In a similar way, the rest of represented modes aim to reproduce the energy increase observed in the frequencies comprised among 8.5-13 kHz and 15-20 kHz. Again, this proves how the pressure field changes its spatial distribution as the frequencies which are exited vary. On the other hand, it is interesting to note that energy of the modes is progressively concentrated within the bowl as the frequency increases, going from completely squish-dominated modes at 5-8.5 kHz to entirely inside-bowl oscillations at 15-20 kHz meanwhile a mixing effect of both regions is easily identifiable at 8.5-13 kHz.

Continuing this comparison, Fig. 15 also includes the time evolution of these specific modes, in an attempt to find possible relationships between the inception of the modes and different phases of the combustion process.

Examination of the first graph exposes how the onset of mode Ψ_1 is coincident with the start of combustion of the first pilot. Moreover, the amplitude rapidly reaches its maximum value during the second pilot combustion phase. This mode is again excited during the diffusive combustion enhancing its amplitude practically up to the highest value. Mode Ψ'_4 however starts to develop after the onset of the second combustion phase and practically disappears after the first steps of the third combustion stage. This evinces the relevance of the early pilot injections in the resonant noise generation, since they heavily contributes to the excitation of less energetic modes.

Regarding the second graph, both modes Ψ_4 and Ψ'_1 start at the second ignition event, although the amplitude rise is much more pronounced in the mode Ψ'_1 while in mode Ψ_4 the time evolution is essentially constant during the whole combustion. Furthermore, the mode Ψ'_1 increases its amplitude during the main combustion stage, reaching its maximum value after 10 cad of the TDC.

Finally, the last graph shows the evolution of Ψ_8 and Ψ'_5 modes. Mode Ψ'_5 displays an amplitude rise at the start of the last two combustion phases but its intensity is severely attenuated due to its high characteristic frequencies. On the other hand, mode Ψ_8 shows a little relevance after the second combustion onset, only exhibiting a significant amplitude during this short stage.

Summary and Conclusions

In this paper, a numerical methodology for optimizing the combustion system of an internal combustion engine has been proposed, with the target of controlling combustion noise while pollutant emissions and performance are maintained, or even improved. This methodology is based on a combination of a genetic algorithm methods and a CFD model specifically implemented to accurately assess the source of combustion noise emissions. Therefore, special attention has been put on recreating the frequency response of the pressure field within the combustion chamber.

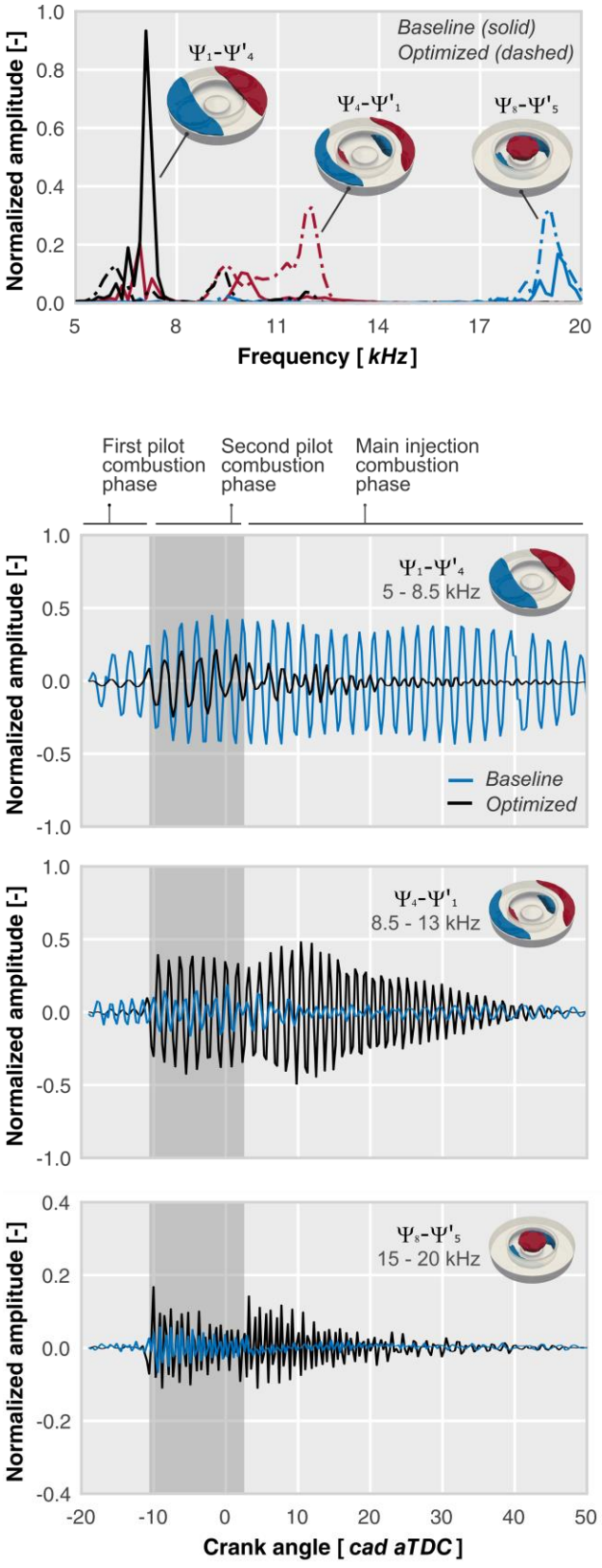

Figure 15. Normalized amplitude of POD modes $\Psi_{1,4,8}$ and $\Psi'_{4,1,5}$ in the frequency (top) and time (bottom) domains. The different combustion phases are also identified to connect possible combustion features with temporary changes in the time evolution of each mode.

Advantage was taken of this methodology to optimize the combustion system design of a CI Diesel engine where the chamber geometry, injector specifications and intake ports design were modified in order to promote a quieter engine design by minimizing high frequency pressure oscillations. The new system is able to reduce noise emissions thanks to a lowering of the resonant contribution, since it establishes the frequency content to feature higher frequencies, less perceptible by the human hearing.

The optimized design included a deeper and tighter bowl geometry with higher swirl and greater number of nozzle holes with smaller nozzle diameters. Thereby, the changes in the injector and intake ports are specially focused to enhance the mixing rate and to minimize the spray penetration, avoiding thus an excessive wall fuel impingement during the injection event. Moreover, the included spray angle increased in order to match with the new bowl geometry.

In addition, an exhaustive analysis of in-cylinder acoustic effects have been presented to understand the unsteady pressure field behavior and to identify the most relevant noise issues. POD decomposition of the baseline and optimized designs was performed, revealing the energy shifting between modes as a result of the different combustion system features. The most dominant mode, and thus the main source of resonant emissions, is hardly attenuated whereas the amplitude of higher order modes are accordingly increased, but never reaching the levels of the first one. Besides the frequency shift, the pressure field also experiences a spatial distribution change. Specifically, the spectral content at 5-8.5 kHz is related to the squish-dominated pulsation, with the 8.5-13 kHz features squish-bowl interaction and the higher frequency content at 15-20 kHz is related to central top-down bowl oscillations. Finally, a relation between the inception of the modes and different phases of the combustion has been identified, showing how early pilot injections severely contributes to the excitation of less energetic modes.

In summary, the methodology presented has permitted to identify the optimization path for diminishing the combustion noise by acting on the acoustic source. The subsequent acoustic analysis has provided interesting conclusions about unexplored phenomena such as those related to the resonant pressure oscillations within the combustion chamber. Lastly, the suitability of the optimization and analysis methodologies has been demonstrated and both can be applied to different engine configurations and combustion concepts in further investigations.

References

1. Kampa, M. and Castanas, E., "Human health effects of air pollution," 4th International Workshop on Biomonitoring of Atmospheric Pollution, 151(2): 362-367, 2008, doi:10.1016/j.envpol.2007.06.012
2. "CDP Global Climate Change Report 2015," Carbon Disclosure Project, 2015.
3. Hasegawa, R., and Yanagihara, H., "HCCI combustion in DI diesel engine," SAE Technical Paper 2003-01-0745, 2003, doi:10.4271/2003-01-0745.
4. Hardy, W. L., and Reitz, R. D., "A study of the effects of high EGR, high equivalence ratio, and mixing time on emissions levels in a heavy-duty diesel engine for PCCI combustion," SAE Technical Paper 2006-01-0026, 2006, doi:10.4271/2006-01-0026.
5. Hanson, R., Splitter, D., and Reitz, R. D., "Operating a heavy-duty direct-injection compression-ignition engine with gasoline for low emissions," SAE Technical Paper 2009-01-1442, 2009, doi:10.4271/2009-01-1442.
6. Manente, V., Johansson, B., Tunestal, P., and Cannella, W., "Effects of Different Type of Gasoline Fuels on Heavy Duty Partially Premixed Combustion," *SAE Int. J. Engines* 2(2):71-88, 2010, doi:10.4271/2009-01-2668.
7. Masterton, B., Heffner, H., and Ravizza, R., "The evolution of human hearing," The Journal of the Acoustical Society of America 45(4):966-985, 1969, doi:10.1121/1.1911574.
8. Schwarz, A. and Janicka, J., "Combustion Noise," Springer-Verlag, Berlin, 2009.
9. Strahle, W. C., "Combustion noise," Progress in Energy and Combustion Science 4(3):157-176, 1978, doi:10.1016/0360-1285(78)90002-3.
10. Flemming, F., Sadiki, A., and Janicka, J., "Investigation of combustion noise using a LES/CAA hybrid approach" Proceedings of the Combustion Institute 31(2):3189-3196, 2007, doi:10.1016/j.proci.2006.07.060.
11. Ren, Y., Randall, R. B., and Milton, B. E., "Influence of the resonant frequency on the control of knock in diesel engines," Proceedings of the Institution of Mechanical Engineers, Part D: Journal of Automobile Engineering 213(2):127-133, 1999, doi:10.1243/0954407991526748.
12. Torregrosa, A. J., Broatch, A., Martín, J., and Monelletta, L., "Combustion noise level assessment in direct injection Diesel engines by means of in-cylinder pressure components," Measurement Science and Technology, 18(7):21-31, 2007, doi:10.1088/0957-0233/18/7/045.
13. Payri, F., Broatch, A., Margot, X., and Monelletta, L., "Sound quality assessment of diesel combustion noise using in-cylinder pressure components," Measurement Science and Technology, 20(1):01-12, 2009, doi:10.1088/0957-0233/20/1/015107.
14. Payri, F., Torregrosa, A. J., Broatch, A., and Monelletta, L., "Assessment of diesel combustion noise overall level in transient operation," International Journal of Automotive Technology, 10(6):761, 2009, doi:10.1007/s12239-009-0089-y.
15. Stanković, L., and Böhme, J. F., "Time–frequency analysis of multiple resonances in combustion engine signals," Signal Processing 79(1):15-28, 1999, doi:10.1016/S0165-1684(99)00077-8.
16. Singh, O. P., Sreenivasulu, T., and Kannan, M., "The effect of rubber dampers on engine's NVH and thermal performance," Applied Acoustics 75:17-26, 2014, doi:10.1016/j.apacoust.2013.07.007.
17. Anderton, D., "Relation between combustion system and engine noise," SAE Technical Paper 790270, 1979, doi:10.4271/790270.
18. Liu, H., Zhang, J., Guo, P., Bi, F., Yu, H., and Ni, G., "Sound quality prediction for engine-radiated noise," Mechanical Systems and Signal Processing 56:277-287, 2015, doi:10.1016/j.ymssp.2014.10.005.
19. Vressner, A., Lundin, A., Christensen, M., Tunestål, P. and Johansson, B., "Pressure oscillations during rapid HCCI combustion," SAE Technical Paper 2003-01-3217, 2003, doi:10.4271/2003-01-3217.
20. Hickling, R. Feldmaier. D.A., and Sung, S.H., "Knock-induced cavity resonances in open chamber diesel engines," Acoust Soc Am 65(5):1474-9, 1979, doi:10.1121/1.382910.
21. Broatch, A., Margot, X., Novella, R., and Gomez-Soriano, J., "Combustion noise analysis of partially premixed combustion concept using gasoline fuel in a 2-stroke engine," Energy 107: 612-624, 2016, doi:10.1016/j.energy.2016.04.045.
22. Broatch, A., Margot, X., Novella, R., and Gomez-Soriano, J., "Impact of the injector design on the combustion noise of gasoline partially premixed combustion in a 2-stroke engine,"

Applied Thermal Engineering 119:530-540, 2017, doi:10.1016/j.applthermaleng.2017.03.081.
23. Torregrosa, A.J., Broatch, A., Margot, X. and Marant, V., "Combustion chamber resonances in direct injection automotive Diesel engines: a numerical approach," International Journal of Engine Research 5(1):83-91, 2003, doi:10.1243/146808704772914264.
24. Benajes, J., Novella, R., Pastor, J. M., Hernández-López, A. et al., "Optimization of the combustion system of a medium duty direct injection diesel engine by combining CFD modeling with experimental validation," Energy Conversion and Management 110:212-229, 2016, doi:10.1016/j.enconman.2015.12.010.
25. Hiroyasu, H., Miao, H., Hiroyasu, T., Miki, M., et al., "Genetic algorithms optimization of diesel engine emissions and fuel efficiency with air swirl, EGR, injection timing and multiple injections," SAE Technical Paper 2003-01-1853, 2003, doi:10.4271/2003-01-1853.
26. Costa, M., Bianchi, G. M., Forte, C., and Cazzoli, G., "A numerical methodology for the multi-objective optimization of the DI diesel engine combustion," Energy Procedia 45:711-720, 2014, doi:10.1016/j.egypro.2014.01.076.
27. Park, S. W., "Optimization of combustion chamber geometry for stoichiometric diesel combustion using a micro genetic algorithm," Fuel Processing Technology 91(11):1742-1752, 2010, doi:10.1016/j.fuproc.2010.07.015.
28. Wickman, D., Yun, H., and Reitz, R., "Split-Spray Piston Geometry Optimized for HSDI Diesel Engine Combustion," SAE Technical Paper 2003-01-0348, 2003, doi:10.4271/2003-01-0348.
29. de Risi, A., Donateo, T., and Laforgia, D., "Optimization of the Combustion Chamber of Direct Injection Diesel Engines," SAE Technical Paper 2003-01-1064, 2003, doi:10.4271/2003-01-1064.
30. Sun, Y., Wang, T., Lu, Z., Cui, L. et al., "The Optimization of Intake Port using Genetic Algorithm and Artificial Neural Network for Gasoline Engines," SAE Technical Paper 2015-01-1353, 2015, doi:10.4271/2015-01-1353.
31. Payri, F., Olmeda, P., Martín, J., and García, A., "A complete 0D thermodynamic predictive model for direct injection diesel engines," Applied Energy 88(12):4632-4641, 2011, doi:10.1016/j.apenergy.2011.06.005.
32. CONVERGENT SCIENCE Inc., "CONVERGE 2.2 Theory Manual," 2015.
33. Ihlenburg, F., "The medium-frequency range in computational acoustics: Practical and numerical aspects," Journal of Computational Acoustics 11(02):175-193, 2003, doi:10.1142/S0218396X03001900.
34. Yakhot, V. and Orszag, S., "Renormalization group analysis of turbulence," Journal of Scientific Computing 1(1):3-51, 1986, doi:10.1007/BF01061452.
35. Angelberger, C., Poinsot, T., and Delhay, B., "Improving Near-Wall Combustion and Wall Heat Transfer Modeling in SI Engine Computations," SAE Technical Paper 972881, 1997, doi:10.4271/972881.
36. Som, S., and Aggarwal, S. K., "Effects of primary breakup modeling on spray and combustion characteristics of compression ignition engines," Combustion and Flame 157(6):1179-1193, 2010, doi:10.1016/j.combustflame.2010.02.018.
37. Moiz, A. A., Ameen, M. M., Lee, S. Y., and Som, S., "Study of soot production for double injections of n-dodecane in CI engine-like conditions," Combustion and Flame 173:123-131, 2016, doi:10.1016/j.combustflame.2016.08.005.
38. Wright, Y. M., Margari, O. N., Boulouchos, K., De Paola, G., et al., "Experiments and simulations of n-heptane spray auto-ignition in a closed combustion chamber at diesel engine conditions," Flow, turbulence and combustion 84(1):49-78, 2010, doi:10.1007/s10494-009-9224-0.
39. Han, Z., and Reitz, R. D., "Turbulence modeling of internal combustion engines using RNG κ-ε models," Combustion science and technology 106(4-6):267-295, 1995, doi:10.1080/00102209508907782.
40. Redlich, O., and Kwong, J. N., "On the Thermodynamics of Solutions. V. An Equation of State. Fugacities of Gaseous Solutions," Chemical reviews 44(1):233-244, 1949, doi:10.1021/cr60137a013.
41. Senecal, P., Pomraning, E., Richards, K., Briggs, T. et al., "Multi-Dimensional Modeling of Direct-Injection Diesel Spray Liquid Length and Flame Lift-off Length using CFD and Parallel Detailed Chemistry," SAE Technical Paper 2003-01-1043, 2003, doi:10.4271/2003-01-1043.
42. Issa, R., "Solution of the implicitly discretised fluid flow equations by operator-splitting," Journal of Computational Physics 62:40-65, 1986, doi:10.1016/0021-9991(86)90099-9.
43. Brakora, J. and Reitz, R., "A Comprehensive Combustion Model for Biodiesel-Fueled Engine Simulations," SAE Technical Paper 2013-01-1099, 2013, doi:10.4271/2013-01-1099.
44. Dukowicz, J.K., "A particle-fluid numerical model for liquid sprays," Journal of Computational Physics 35(2):229-253, 1980, doi:10.1016/0021-9991(80)90087-X.
45. Reitz, R.D. and Beale, J.C., "Modeling spray atomization with the kelvin-helmholtz /rayleigh-taylor hybrid model," Atomization and Sprays 9(6):623-650, 1999, doi:10.1615/AtomizSpr.v9.i6.40.
46. Torregrosa, A.J., Olmeda, O., Degraeuwe, B. and Reyes, M., "A concise wall temperature model for DI diesel engines," Applied Thermal Engineering 26 (11:12):1320-1327, 2006, doi:10.1016/j.applthermaleng.2005.10.021.
47. Navid, A., Khalilarya, S., and Taghavifar, H., "Comparing multi-objective non-evolutionary NLPQL and evolutionary genetic algorithm optimization of a DI diesel engine: DoE estimation and creating surrogate model," Energy Conversion and Management 126:385-399, 2016, doi:10.1016/j.enconman.2016.08.014.
48. Griffiths, A. J., Miller, J. H., Suzuki, D. T., Lewontin, R. C., et al. Selective systems, 2000.
49. Torregrosa, A. J., Broatch, A., Margot, X., and Gomez-Soriano, J., "Towards a Predictive CFD Approach for Assessing Noise in Diesel Compression Ignition Engines. Impact of the Combustion Strategies," paper presented at the International Conference on Modeling and Diagnostics for Advanced Engine systems: the 9th COMODIA, Okayama (Japan), 2017.
50. Singh, O. P., Sreenivasulu, T., and Kannan, M. "The effect of rubber dampers on engine's NVH and thermal performance," Applied Acoustics 75:17-26, 2014, doi:10.1016/j.apacoust.2013.07.007.
51. Torregrosa, A. J., Broatch, A., Novella, R., Gomez-Soriano, J., et al. "Impact of gasoline and Diesel blends on combustion noise and pollutant emissions in Premixed Charge Compression Ignition engines," Energy 137:58-68, 2017, doi:10.1016/j.energy.2017.07.010.
52. Desantes, J., Torregrosa, A., and Broatch, A., "Wavelet Transform applied to Combustion Noise Analysis in High-speed DI Diesel Engines," SAE Technical Paper 2001-01-1545, 2001, doi:10.4271/2001-01-1545.
53. Huang, Y., and Yang, V. "Dynamics and stability of lean-premixed swirl-stabilized combustion," Progress in energy and combustion science 35(4):293-364, 2009, doi:10.1016/j.pecs.2009.01.002.

54. Steinberg, A. M., Boxx, I., Stöhr, M., Carter, C. D., et al., "Flow–flame interactions causing acoustically coupled heat release fluctuations in a thermo-acoustically unstable gas turbine model combustor," Combustion and Flame 157(12):2250-2266, 2010, doi:10.1016/j.combustflame.2010.07.011.
55. Kostka, S., Lynch, A. C., Huelskamp, B. C., Kiel, B. V., et al., "Characterization of flame-shedding behavior behind a bluff-body using proper orthogonal decomposition," Combustion and Flame 159(9):2872-2882, 2012, doi:10.1016/j.combustflame.2012.03.021.
56. Liang, Y. C., Lee, H. P., Lim, S. P., Lin, W. Z. et al., "Proper orthogonal decomposition and its applications-Part I: Theory," Journal of Sound and vibration 252(3):527-544, 2002, doi:10.1006/jsvi.2001.4041.
57. Bizon, K., Continillo, G., Mancaruso, E., Merola, S. S., et al., "POD-based analysis of combustion images in optically accessible engines," Combustion and flame 157(4):632-640, 2010, doi:10.1016/j.combustflame.2009.12.013.
58. Chen, H., Hung, D. L., Xu, M., Zhuang, H., et al., "Proper orthogonal decomposition analysis of fuel spray structure variation in a spark-ignition direct-injection optical engine," Experiments in fluids 55(4):1703, 2014, doi:10.1007/s00348-014-1703-y.
59. Chen, H., Reuss, D. L., and Sick, V., "Analysis of misfires in a direct injection engine using proper orthogonal decomposition" Experiments in fluids 51(4)1139, 2011, doi:10.1007/s00348-011-1133-z.
60. Danby, S. J., and Echekki, T., "Proper orthogonal decomposition analysis of autoignition simulation data of nonhomogeneous hydrogen–air mixtures," Combustion and flame 144(1):126-138, 2006, doi:10.1016/j.combustflame.2005.06.014.
61. Torregrosa, A. J., Broatch, A., García-Tíscar, J., and Gomez-Soriano, J., "Modal decomposition of the unsteady flow field in compression-ignited combustion chambers," Combustion and flame XX(X):XXX-XXX, 2017, doi:XXXX.
62. Payri, F., Broatch, A., Tormos, B., and Marant, V., "New methodology for in-cylinder pressure analysis in direct injection diesel engines—application to combustion noise," Measurement Science and Technology 16(2):540, 2005, doi:10.1088/0957-0233/16/2/029.

Contact Information

Ricardo Novella Ph.D.
CMT - Motores Térmicos
Universidad Politécnica de Valencia
rinoro@mot.upv.es

Acknowledgments

The equipment used in this work has been partially supported by FEDER and the Spanish Government through grant no. DPI2015-70464-R and by FEDER project funds "Dotación de infraestructuras científico técnicas para el Centro Integral de Mejora Energética y Medioambiental de Sistemas de Transporte (CiMeT), (FEDER-ICTS-2012-06)", framed in the operational program of unique scientific and technical infrastructure of the Spanish Ministerio de Economía y Competitividad.

J. Gomez-Soriano is partially supported through contract FPI-S2-2016-1353 of the "Programa de Apoyo para la Investigación y Desarrollo (PAID-01-16)" of Universitat Politècnica de València.

The authors want to express their gratitude to CONVERGENT SCIENCE Inc. and IGNITE3D Engineering GmbH for their kind support for performing the CFD calculations using CONVERGE software.

Abbreviations

AMR	Adaptive Mesh Refinement
aTDC	After Top Dead Centre
BDC	Bottom Dead Centre
cad	Crank angle degree
CDC	Conventional Diesel Combustion
CFD	Computational fluid dynamics
CI	Compression Ignition
DDM	Discrete Droplet Model
DI	Direct Injection
EGR	Exhaust Gases Recirculation
EVO	Exhaust Valve Opening (angle)
FFT	Fast Fourier Transform
GA	Genetic Algorithm
GCI	Gasoline Compression Ignition
GEP	Gas Exchange Process
HCCI	Homogeneous Charge Compression Ignition
HSDI	High Speed Direct Injection
ICE	Internal Combustion Engine
ISFC	Indicated specific fuel consumption
IVC	Intake Valve Closing (angle)

KHRT	Kelvin-Helmholtz Rayleigh-Taylor
MF	Merit Function
NVH	Noise, Vibration and Harshness
ON	Overall engine Noise
PCA	Principal Component analysis
PISO	Pressure Implicit with Splitting of Operators
PM	Particulate Matter
POD	Proper Orthogonal Decomposition
PRF	Primary Reference Fuel
RoHR	Rate of Heat Release
SD	Standard deviation
SI	Spark Ignition
SoI	Start of Injection (angle)
SPL	Sound pressure level
TDC	Top Dead Centre

Appendix

The characterization of the combustion noise used in this paper is based on the in-cylinder pressure decomposition proposed by Payri et al. [62]. According to this method, it is possible to identify three frequency bands in the pressure spectrum, each linked to one of the three engine cycle parts: compression-expansion phase, combustion event and resonance phenomenon. This procedure also allows to identify which parameters are those most influential in each frequency band. Taking advantage of this information, subsequent investigations [12,13] have found cause-effect relations between the source and both the objective and subjective effects of noise. Torregrosa et al. [12] have demonstrated the relation between the engine radiated noise or ON and three indicators: one operation indicator which quantifies the effect of the engine speed, and two combustion indicators that represent the in-cylinder pressure rise and the high frequency gas oscillation inside the combustion chamber, respectively. Then, the overall noise can be obtained by

$$\mathrm{ON} = C_0 + C_n I_n + C_1 I_1 + C_2 I_2 \tag{2}$$

where Ci are coefficients which depend on the engine concept and size. These coefficients were also determined by Torregrosa et al. [12], who obtained the most convenient correlation coefficients to link the noise source with the engine radiated noise through a multiple regression analysis.

The indicators Ii are considered as fundamental noise parameters and are linked to a specific bandwidth of frequencies in the response of the source. The operation indicator (In), associated with the low frequencies, depends on both the engine speed (n) and the idle speed (nidle) as

$$I_n = \log\left[\frac{n}{n_{\mathrm{idle}}}\right] \tag{3}$$

The combustion indicator (I1) characterises the sudden pressure rise due to the combustion and it is related to the medium bandwidth of frequencies. Hence, it is defined as

$$I_1 = \frac{n}{n_{\mathrm{idle}}}\left[\frac{(\mathrm{d}p/\mathrm{d}t)^{\max_1}_{\mathrm{comb}} + (\mathrm{d}p/\mathrm{d}t)^{\max_2}_{\mathrm{comb}}}{(\mathrm{d}p/\mathrm{d}t)^{\max}_{\mathrm{comp}}}\right] \tag{4}$$

where (dp/dt)maxi are the two maximum peak values of the pressure rise rate during the combustion. The parameter (dp/dt)p-mot is the maximum peak value of the pressure rise rate of the pseudo-motored signal.

Finally, the resonance indicator (I2) represents the contribution of the resonance phenomena inside the chamber. It is mathematically expressed as

$$I_2 = \log\left[E_0 \frac{E_{\mathrm{res}}}{E_{\mathrm{comp}}}\right] \tag{5}$$

Here E0 is a convenient scaling factor and Eres is the signal energy of the resonance pressure oscillations. This parameter is obtained by evaluating the integral of the resonant oscillations, p(t)res, between the IVC and EVO as

$$E_{\mathrm{res}} = \int_{\mathrm{IVC}}^{\mathrm{EVO}} p(t)^2_{\mathrm{res}}\,\mathrm{d}t \tag{6}$$

The resonance signal, p(t)res, may be identified by high-pass filtering of the in-cylinder pressure. The filter cut-off frequency is fixed by an empirical function, which depends on the engine speed [25]:

$$f_{cut} = 2.364 \cdot n - 2.91 \cdot 10^{-4} \cdot n^2 \tag{7}$$

Similarly, Ep-mot is the energy of the pseudo-motored signal and it can be obtained by assessing the following integral between IVC and EVO.